ACS OMEGA

http://pubs.acs.org/journal/acsodf

Article

# Synthesis and Characterization of Thermosensitive P(NIPAAm-*co*-AAc)-Grafted Silica Nanocomposites for Smart Architectural Coatings

Chien-Chen Diao and Chia-Ching Wu*

Cite This: *ACS Omega* 2022, 7, 8697−8705

Read Online

ACCESS | Metrics & More | Article Recommendations | Supporting Information

**ABSTRACT:** In this study, a new class of thermosensitive poly(*N*-isopropylacrylamide)-*co*-poly(acrylic acid) (P(NIPAAm-*co*-AAc))-grafted modified silica (m-silica) nanocomposites was prepared using a sol−gel technique. The addition of silica to P(NIPAAm-*co*-AAc) copolymer hydrogel has the potential to open up new applications in the development of thermosensitive building materials by leveraging the favorable thermal characteristics of P(NIPAAm-*co*-AAc). The silica was prepared using 3-aminopropyltriethoxysilane and 4,4′-azobis(4-cyanovaleric acid) to form the m-silica powder, which increased the adhesion between the organic and inorganic hybrid materials. The P(NIPAAm-*co*-AAc) copolymer hydrogel was mixed with the m-silica to form the P(NIPAAm-*co*-AAc)-grafted m-silica nanocomposites. Scanning electron microscopy, X-ray diffraction analysis, thermogravimetric analysis, Fourier-transform infrared spectroscopy, and thermosensitive measurement were conducted to evaluate the structure and water-holding capacity of the nanocomposites. The results indicated that the P(NIPAAm-*co*-AAc)-grafted m-silica nanocomposites could retain water for more than 300 min at temperatures higher than the lower critical solution temperature. The P(NIPAAm-*co*-AAc)-grafted m-silica nanocomposites exhibited favorable thermosensitive properties and may therefore be applied in smart architectural coatings.

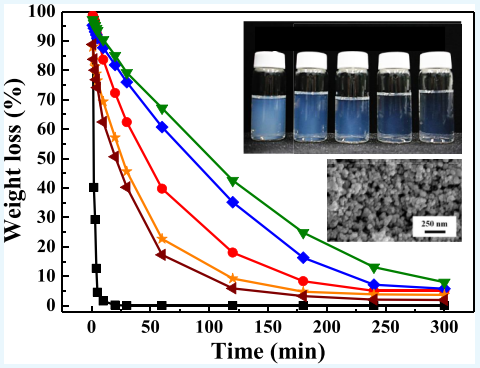


## INTRODUCTION

Greenhouse gas (GHG) emissions have become a key environmental and climate change concern.[1] The three major contributors to GHG emissions are buildings, industry, and transportation.[2] In architecture, an increase in the area of the exterior wall covered by artificial materials leads to a greater heat absorption capacity. However, the heat absorbed by artificial materials does not dissipate easily; this increases the use of indoor air conditioning and GHG emissions and leads to a warmer environment. Therefore, controlling increases in environmental temperatures is a key strategy for mediating the greenhouse effect.[3] Some countermeasures must be implemented to control the trend toward an unlivable climate. Roofs and walls receive stronger direct radiation from the sun for longer periods than do other parts of buildings, and approximately 70% of heat gained in top floor rooms comes through roofs and walls.[4] Therefore, having plants on the roofs of buildings (i.e., green roofing) and using water-retentive materials in construction can result in cooler buildings through transpiration and evaporation, respectively.[5,6]

Most materials used in the exterior walls of buildings are made from porous ceramics. Compared with dense ceramics, porous ceramics not only are more lightweight and highly machinable but also exhibit greater sound absorption, heat insulation, and water retention. The cooling effect achieved by the evaporation of absorbed water from porous ceramic materials can be used to cool buildings. Water-retentive materials can thus maintain the desired indoor temperature and decrease the use of air conditioning when used in construction. Therefore, researchers have attempted to tailor the properties of porous ceramics for use in the construction industry.[7−9]

Porous ceramic materials have been developed from several materials such as alumina, low-grade silica, cordierite, glass, and some silicate waste materials.[10−16] The water retention properties of porous ceramics depend on the ceramic's pore size; larger pores result in higher water absorption and water release rates.[17,18] However, the water retention performance of water-retentive materials with large pore sizes gradually decreases after the temperature increases in the morning and cannot be sustained when the temperature peaks at noon. The pore size of porous ceramic materials has been demonstrated to be affected by the sintering temperature of the specific

Received: November 30, 2021
Accepted: January 28, 2022
Published: March 2, 2022





https://doi.org/10.1021/acsomega.1c06776
*ACS Omega* 2022, 7, 8697−8705

material used. In general, porous ceramic materials must be sintered at high temperatures (>800 °C).[8,19−23] However, the material synthesized at high temperatures wastes energy.

*N*-Isopropylacrylamide (NIPAAm) is a typical thermosensitive hydrogel that exhibits a volume−phase transition at approximately 32 °C (its lower critical solution temperature [LCST]).[24] Below this temperature, the hydrogel becomes swollen, hydrated, and hydrophilic, whereas at temperatures above the LCST, the hydrogel shrinks and becomes collapsed, dehydrated, and hydrophobic due to the breakdown of the delicate hydrophilic−hydrophobic balance in the gel network.[25] This distinctive property of NIPAAm is attributable to its unique rapid alternations between hydrophilicity and hydrophobicity at temperatures near its LCST.[26] The unique phase transition of NIPAAm hydrogels in response to external temperature changes has been widely investigated.[27] Many studies on NIPAAm hydrogels have focused on applications in controlled drug delivery,[28] enzyme activity regulation,[23] and thermocontrolled chromatography.[29]

In previous studies, acrylic acid (AAc) has often been copolymerized with NIPAAm as a pH-sensitive component to regulate the properties of P(NIPAAm-*co*-AAc) copolymer hydrogels. Copolymerization with AAc can also introduce a side carboxyl group into the copolymer, which can further react with other molecules for many applications. AAc is hydrophilic and can increase the volume−phase transition temperature; therefore, combining different contents of AAc with NIPAAm can change the LCST, swelling behavior, and release rate of NIPAAm. One strategy for achieving this aim involves copolymerizing NIPAAm with AAc to form poly(*N*-isopropylacrylamide)-*co*-poly(acrylic acid) (P(NIPAAm-*co*-AAc)) copolymer hydrogels.[30−36]

In this study, we used different contents of AAc mixed with NIPAAm to form P(NIPAAm-*co*-AAc) hydrogels and obtained different LCSTs of the P(NIPAAm-*co*-AAc) copolymer hydrogels. The P(NIPAAm-*co*-AAc) copolymer hydrogels were selected as the water-retentive material to be used in architectural applications. P(NIPAAm-*co*-AAc) copolymer hydrogels can absorb moisture and dew at night, and the water is released at approximately noon when the temperature surpasses the LCST of P(NIPAAm-*co*-AAc) copolymer hydrogels. However, because average daytime temperatures vary by region, controlling the LCST of the P(NIPAAm-*co*-AAc) copolymer hydrogels is key to enhancing the applicability of water-retentive building materials.

Most building materials contain silica, and to ensure the compatibility of the P(NIPAAm-*co*-AAc) copolymer hydrogels with typical building materials, the hydrogels were mixed with silica to form nanocomposites to be used in smart architectural coatings. However, the silica surface contains numerous silanol groups, which form bonds to create silica aggregates. This agglomeration behavior can reduce the benefits afforded by these materials. Therefore, modifying the silica surface to make it compatible with another phase is essential. Several approaches, including physical (physisorption) and chemical (covalent bonding) methods and graft polymerization, are used to modify the surface of the silica.[37−41] Methods for grafting polymer chains onto silica surfaces include terminating growing chains on surface-active groups, copolymerizing immobilized double bonds, and initiating polymerization with immobilized initiators. These various grafted chains serve as active precursors in radical polymerization, and all these chains can be coupled to the silica surfaces through the solution deposition of functionalized silanes.[42−45] Therefore, different contents of 3-aminopropyltriethoxysilane (APTES) and 4,4′-azobis(4-cyanovaleric acid) (ACVA)-modified silica (m-silica) were mixed with hydrogel copolymers to form absorbent/releasing P(NIPAAm-*co*-AAc)-grafted m-silica nanocomposites in this study. The P(NIPAAm-*co*-AAc)-grafted m-silica nanocomposites absorb moisture and dew at night; in the morning, when the ambient temperature is lower than the LCST of the nanocomposites, the nanocomposites retain water and maintain low temperatures inside the building. At approximately noon, when the ambient temperature is higher than the LCST of the nanocomposites, moisture can be released, which helps maintain low temperatures inside the building, thereby reducing the use of cooling equipment and, in turn, reducing GHG emissions. In addition, compared with the synthesis of the porous ceramic materials, the P(NIPAAm-*co*-AAc)-grafted m-silica nanocomposites synthesized at low temperatures can save energy during the fabrication process. Therefore, nanocomposites can be applied in smart architectural coatings.

## EXPERIMENTAL DETAILS

**Materials.** The following reagents were purchased and used without further purification: *N*-isopropylacrylamide, which was used as the hydrogel monomer (97%, NIPAAm, Sigma-Aldrich); AAc (99%, Sigma-Aldrich), which was used as the comonomer; ammonium persulfate (99%, APS, Sigma-Aldrich), which was used as the initiator; *N*,*N*-methylenebisacrylamide (NMBA, 99%, Sigma-Aldrich), which was used as the crosslinker; *N*,*N*,*N*′,*N*′-tetramethyl ethylene diamine (99%, TMEDA, Alfa Aesar), which was used as the activator; and APTES (99%, Sigma-Aldrich), which was used as the coupling agent. ACVA, tetrahydrofuran (THF), and ethyl chloroformate (ECF) were purchased from Sigma-Aldrich; triethylamine (TEA) was purchased from Alfa Aesar; and toluene, benzene, and ethanol were purchased from Uni-Onward (New Taipei City, Taiwan). Deionized water was used throughout the hydrogel preparation and swelling processes.

**P(NIPAAm-*co*-AAc) Copolymer Hydrogel Synthesis.** The P(NIPAAm-*co*-AAc) copolymer hydrogels were prepared through free radical polymerization. The NIPAAm (3.051 g) and AAc (1−9 mol %) were dissolved in 100 mL of deionized water in a three-necked round-bottom flask equipped with a nitrogen inlet and underwent nitrogen bubbling for 15 min. APS (0.132 g) was placed in another three-necked round-bottom flask and stirred at 120 rpm. The predissolved NIPAAm and AAc were then added to the APS reaction vessel with the crosslinker (0.249 g of NMBA). Finally, 0.2 mL of TMEDA was added, and the mixture was stirred for 5 min. Free radical copolymerization of the P(NIPAAm-*co*-AAc) copolymer hydrogels was conducted in glass tubes at room temperature for 24 h, after which the hydrogels were immersed in deionized water that was refreshed every 10 min for five times to allow for the removal of the unreacted monomer.

**Functionalized Silica.** To improve its organic−inorganic interface, the silica powder was modified before being mixed with the P(NIPAAm-*co*-AAc) copolymer hydrogels. A typical procedure for the surface modification of silica with a coupling agent was performed as follows: silica (100 g) was dried at 400 °C for 2 h and placed with 850 mL of toluene under a stream of nitrogen in a glass flask with a reflux condenser. APTES (150 mL) was then introduced, and the solution was stirred under a nitrogen stream at 110 °C for 12 h. The prepared silica


https://doi.org/10.1021/acsomega.1c06776
ACS Omega 2022, 7, 8697−8705

was dried at 200 °C for 2 h and subsequently washed with methanol and water several times. A schematic of the synthetic routes for APTES-silica is presented in Figure 1b.

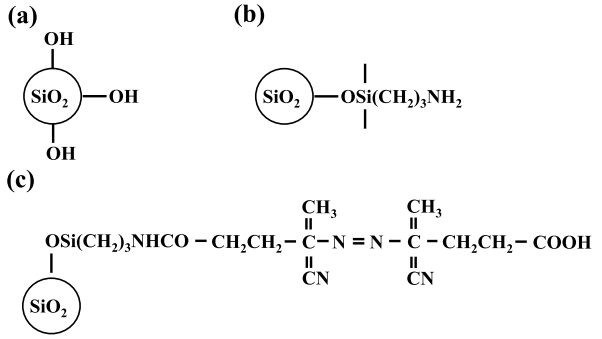


**Figure 1.** Schematic of synthetic routes for modification of silica. (a) unmodified, (b) APTES-modified, and (c) APTES−ACVA-modified.

To perform the reaction between the ACVA and APTES-modified silica, a 500 mL flask was filled with 373 mL of THF. The flask was then cooled to 0 °C. ACVA (7.5 g), ECF (8.2 mL), and TEA (3.3 mL) were sequentially added. After 15 min, APTES-silica (20 g) was introduced to the mixture. After 1 h of reaction, the mixture was refrigerated overnight. The precipitated solid was filtered out; washed with THF, water, and methanol; and dried in a vacuum to produce radical initiator-carrying silica (m-silica), as illustrated in Figure 1c.

**P(NIPAAm-*co*-AAc)-Grafted M-silica Nanocomposites Synthesis.** Before being mixed with the nanosized m-silica powder, 3 mol % AAc was mixed with NIPAAm to form the P(NIPAAm-*co*-3 mol % AAc) copolymer hydrogels. Subsequently, the 10−90 wt % nanosized m-silica powder was mixed with the copolymer hydrogels, and the P(NIPAAm-*co*-3 mol % AAc)-grafted m-silica nanocomposites were thus fabricated.

**Measuring Equipment.** High-resolution scanning electron microscopy (SEM, SU8000, Hitachi Company) at 10 kV was used to examine the P(NIPAAm-*co*-AAc)-grafted m-silica nanocomposites and silica powder morphology. The crystallography of the P(NIPAAm-*co*-AAc)-grafted m-silica nanocomposites was examined through X-ray diffraction (XRD, D8 Discover, Bruker Company) with Cu K$\alpha$ radiation ($2\theta$ = 5−50°). The composition of the resultant P(NIPAAm-*co*-AAc)-grafted m-silica nanocomposite supports was investigated through thermogravimetric analysis (TGA, Q500, TA Instruments). The nanocomposites were heated from room temperature to 800 °C at a rate of 20 °C/min under a nitrogen atmosphere. Functional group analysis of the P(NIPAAm-*co*-AAc) copolymer hydrogels and m-silica was performed using Fourier-transform infrared spectroscopy (FTIR, NEXUS 670, Nicolet Company). The copolymer hydrogels, m-silica, and nanocomposites were ground into a powder, mixed with KBr at a mass ratio of 1 to 80, and pressed into a thin disk. The spectra of KBr-base thin disk were obtained and scanned over a wavenumber range of 500−4000 $cm^{-1}$ at a scan ratio of 0.5 $cm^{-1}$ and repeated 2 times.

**Thermosensitive Measurement of Architectural Coatings.** The P(NIPAAm-*co*-3 mol % AAc)-grafted m-silica nanocomposites were coated on ceramic discs by the screen printing method. The dried nanocomposites with different contents of m-silica coated on the discs were immersed in deionized water for 12 h at a constant temperature until swelling equilibrium was attained. The discs were removed from the water bath and tapped with delicate task wipers to remove excess surface water, and the wet weight of the nanocomposites was measured. The discs were subsequently heated at 40 °C, and the weight loss−time curve was obtained.

## RESULTS AND DISCUSSION

**Characterization of the P(NIPAAm-*co*-AAc) Copolymer Hydrogels.** To increase the LCST of the NIPAAm, P(NIPAAm-*co*-AAc) copolymer hydrogels with different AAc concentrations were fabricated through free radical polymerization. Figure 2 illustrates the FTIR spectra of the

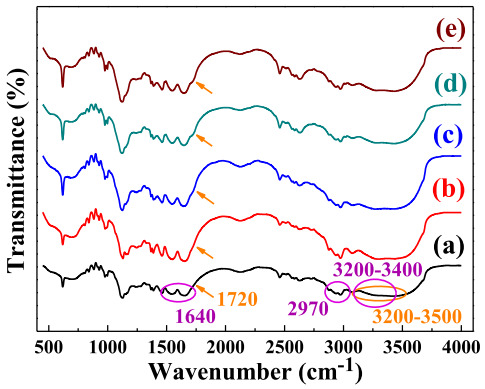


**Figure 2.** FTIR spectra of the P(NIPAAm-*co*-AAc) copolymer hydrogels with different AAc monomer concentrations. (a) 1, (b) 3, (c) 5, (d) 7, and (e) 9 mol %.

P(NIPAAm-*co*-AAc) copolymer hydrogels with different AAc concentrations with a wavenumber range from 4000 to 400 $cm^{-1}$. In Figure 2a, the absorption band of the hydrogel copolymer with 1 mol % AAc at 1720 and 3200−3500 $cm^{-1}$ could be assigned to the C═O and O−H vibration of AAc, respectively. The small wavelength range near 1720 $cm^{-1}$ is shown in Figure S1. The absorption bands at 1640 and 3200−3500 $cm^{-1}$ could be assigned to the C═O and *N*−H vibration of NIPAAm, respectively. The broadband maximum at 1650 $cm^{-1}$ could be assigned to the overlapping NIPAAm and AAc absorptions at 1600−1800 $cm^{-1}$.[46−49] As the AAc concentration increased, the absorption band intensity of the hydrogel copolymer increased, particularly that of the AAc absorption band. Thus, the presence of these bands in the spectrum confirmed the copolymerization reaction between NIPAAm and AAc.

For the equilibrium-swelling ratio variation, the NIPAAm exhibited an expected LCST at 32 °C, as presented in Figure 3. After 1 mol % AAc was added, the P(NIPAAm-*co*-AAc) copolymer hydrogels' LCSTs shifted from 32 °C for NIPAAm to 38 °C for P(NIPAAm-*co*-1 mol % AAc) copolymers. The AAc concentration increased from 3 to 9 mol %, and the LCST of the P(NIPAAm-*co*-AAc) copolymer hydrogels increased from 44 to 68 °C, as shown in Figure 3. Incorporation of ionizable AAc groups in the NIPAAm structure increased their sensitivity to temperature. In addition, the transmittance of the P(NIPAAm-*co*-AAc) copolymer hydrogels at room temperature increased with AAc concentration, as explained in the Figure 3 inset. The transmittance results corresponded to the LCST of the P(NIPAAm-*co*-AAc) copolymer hydrogels with different AAc concentrations.


https://doi.org/10.1021/acsomega.1c06776
ACS Omega 2022, 7, 8697−8705

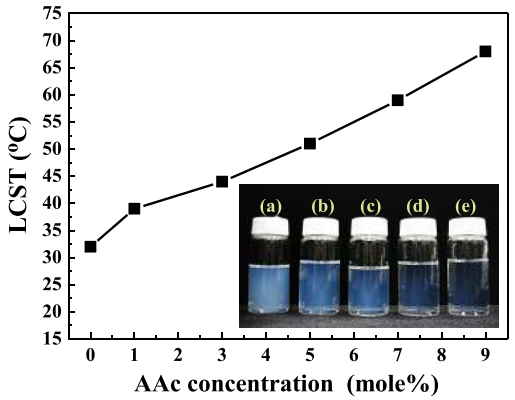


**Figure 3.** LCST analysis of the P(NIPAAm-*co*-AAc) copolymer hydrogels with different AAc concentration. The photograph of the P(NIPAAm-*co*-AAc) copolymer hydrogels with different AAc concentrations at room temperature inset the figure. (a) 1, (b) 3, (c) 5, (d) 7, and (e) 9 mol %.

**Characterization of P(NIPAAm-*co*-AAc)-Grafted M-silica Nanocomposites.** To improve the organic−inorganic interface, the silica powder was modified before being mixed with the P(NIPAAm-*co*-AAc) copolymer hydrogels. Figure 4

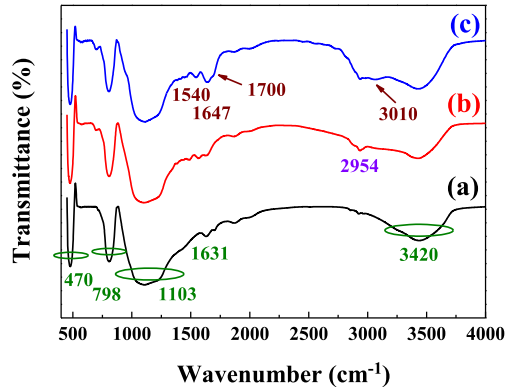


**Figure 4.** FTIR spectra of (a) nonmodified silica, (b) APTES−silica, and (c) APTES−ACVA−silica powder diluted by KBr.

presents the FTIR spectrum for each modification step of the silica powder, with wavenumbers ranging from 4000 to 400 $cm^{-1}$. The absorption bands of the nonmodified silica powder at 470, 798, 1103, 1631, and 3420 $cm^{-1}$ are attributable to the bending vibration of Si−O−Si bonds, symmetric stretching vibration of Si−O−Si bonds, asymmetric stretching vibration of Si−O−Si bonds, silanol stretching bonds, and O−H vibration of the absorbed $H_2O$, respectively, as presented in Figure 4a. After APTES functionalization, Figure 4b reveals that in addition to the peaks of the original silica powder, the APTES-modified silica powder peaked at 2954 $cm^{-1}$ ($CH_2$) and 690 $cm^{-1}$ (deformation of CH out of plane).[50] The APTES−ACVA−silica powder produced new peaks at 1540 $cm^{-1}$ (N−H amide), 1647 $cm^{-1}$ (C═O amide), 1700−1710 $cm^{-1}$ (C═O carboxylic acid), and 2995 $cm^{-1}$ ($CH_3$), as displayed in Figure 4c.[51]

The morphologies of the silica and m-silica powder were examined using SEM, and the results are displayed in Figure 5. Figure 5a shows that the particle size of the silica powder was uniformly distributed between 25 and 45 nm. The particle size

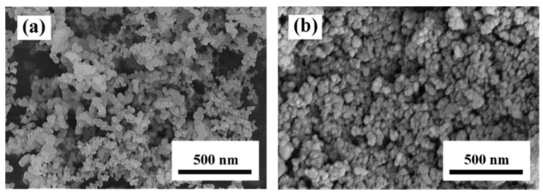


**Figure 5.** SEM images of (a) nonmodified and (b) APTES−ACVA−silica powder.

and morphology of the m-silica powder were the same as those of the silica powder, as indicated in Figure 5b.

To develop smart architectural coatings, the P(NIPAAm-*co*-AAc) copolymer hydrogels were mixed with the m-silica to form the nanocomposites. Taiwan's climate includes temperatures of approximately 36−39 °C at 12 pm. Therefore, the 3 mol % AAc mixture with NIPAAm was selected to form the P(NIPAAm-*co*-3 mol % AAc) copolymer hydrogels. Figure 6a−e displays the surface SEM morphologies of the P(NIPAAm-*co*-3 mol % AAc)-grafted m-silica nanocomposites added to 10, 30, 50, 70, and 90 wt % m-silica powders. The black region in Figure 6a represents the P(NIPAAm-*co*-3 mol % AAc) copolymer hydrogels, and the white and gray particles represent the m-silica powder with 10 wt % content. In Figure 6b,c, the m-silica powder content increased as the number of white and gray particles increased, exhibiting a uniform distribution in the P(NIPAAm-*co*-3 mol % AAc) copolymer hydrogels. The m-silica powder was embedded in the P(NIPAAm-*co*-3 mol % AAc) copolymer hydrogels. As the m-silica powder content increased, the core−shell structure formed as the P(NIPAAm-*co*-3 mol % AAc) copolymer hydrogels coated the m-silica powder surface.

Figure S2 displays the element mapping images of the P(NIPAAm-*co*-3 mol % AAc)-grafted m-silica nanocomposites with different m-silica powder contents. The blue, green, and red points in Figure S2a−g represent carbon, oxygen, and silicon, respectively. The m-silica powder thus was embedded and uniformly dispersed in the P(NIPAAm-*co*-3 mol % AAc) copolymer hydrogels, as presented in Figure S2a−g, and the m-silica in the P(NIPAAm-*co*-3 mol % AAc)-grafted m-silica nanocomposites increased the m-silica content from 10 to 90 wt %. These results correspond with the SEM images displayed in Figure 6.

XRD patterns of the P(NIPAAm-*co*-3 mol % AAc)-grafted m-silica nanocomposites are presented in Figure 7. The diffraction peaks were detected in all P(NIPAAm-*co*-3 mol % AAc)-grafted m-silica nanocomposites with different m-silica powder contents in the same $2\theta$ regions. The diffraction pattern of the NIPAAm-*co*-3 mol % AAc-grafted m-silica nanocomposites with 10 wt % m-silica powder at $2\theta$ values revealed peaks between 7 and 8° and broadband peaks between 16 and 24°, which reflected the NIPAAm and amorphous silica powder (JCPDS 29-0085), as indicated in Figure 7a−e.[52] The first peak of the NIPAAm-*co*-3 mol % AAc-grafted m-silica nanocomposites with the 10 wt % m-silica powder was detected at a $2\theta$ value between 7 and 8°. This peak corresponded to the interplanar distance between associated polymer chains ($d_1$-spacing) of the NIPAAm, as displayed in Figure S3a.

The deconvolution of the second broader band peak to the Gaussian fit for the NIPAAm and m-silica powder peak center were approximately 19 and 22°, respectively. The diffraction peak center from the NIPAAm was revealed at $2\theta$ value 19°


https://doi.org/10.1021/acsomega.1c06776
ACS Omega 2022, 7, 8697−8705

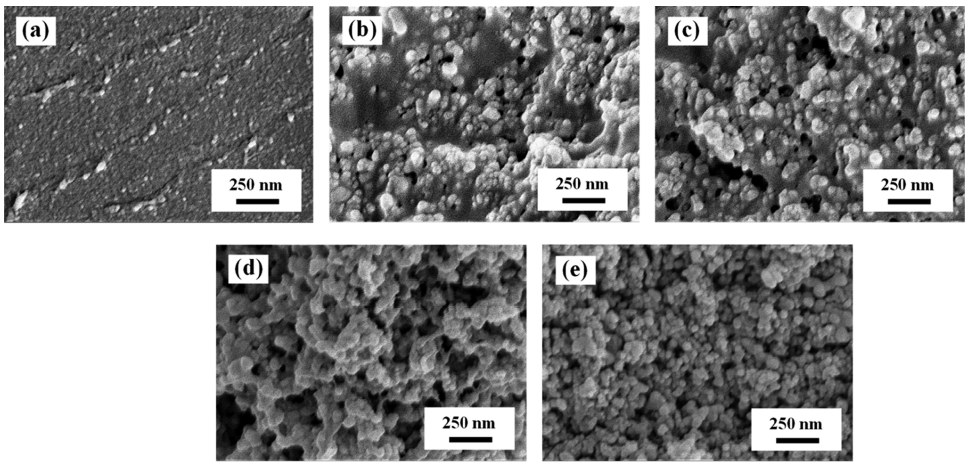


**Figure 6.** SEM images of the P(NIPAAm-*co*-3 mol % AAc)-grafted m-silica nanocomposites with different contents of the m-silica powder contents. (a) 10, (b) 30, (c) 50, (d) 70, and (e) 90 wt %.

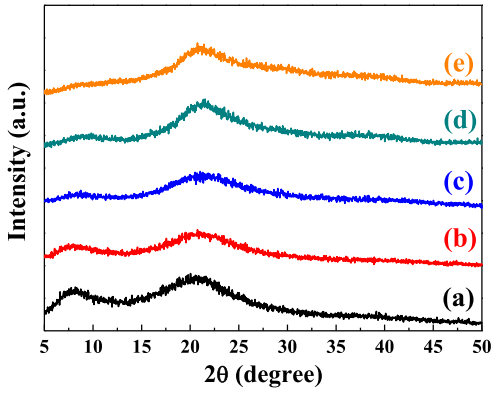


**Figure 7.** XRD patterns of the P(NIPAAm-*co*-3 mol % AAc)-grafted m-silica nanocomposites with different content of the m-silica powder. (a) 10, (b) 30, (c) 50, (d) 70, and (e) 90 wt %.

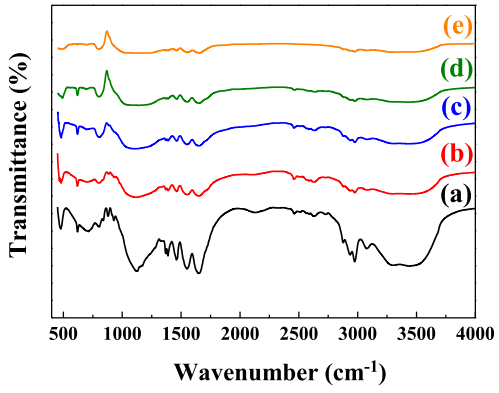


**Figure 8.** FTIR patterns of the P(NIPAAm-*co*-3 mol % AAc)-grafted m-silica nanocomposites with different content of the m-silica powder. (a) 10, (b) 30, (c) 50, (d) 70, and (e) 90 wt %.

and corresponded to the $d_2$-spacing, as expressed in Figure S3b. This peak could not be a multiple of the diffraction peak observed at peaks because of its value (7−8°). The second broader peak represented a structural feature (bond lengths of the backbone and between side chains) of the polymers. In addition, no diffraction peaks of the AAc and second phase are displayed in Figure 7. The diffraction peak intensity at a 2$\theta$ value of 7−8° of the P(NIPAAm-*co*-3 mol % AAc) copolymer hydrogels slightly decreased, and the broadband peak at 16−24° increased as the m-silica powder content increased from 10 to 90 wt %. As the m-silica powder content increased to 90 wt %, so did the intensity of the broad band centered at a 2$\theta$ value of 22°, which was the diffraction peak for amorphous silica, as presented in Figure 7d,e. This indicated that the m-silica powder was embedded in the P(NIPAAm-*co*-3 mol % AAc) copolymer hydrogels as an m-silica content function, and the results corresponded with the SEM images and energy dispersive spectroscopy results (Figures 5 and 6).

Figure 8 presents the FTIR spectra of the P(NIPAAm-*co*-3 mol % AAc)-grafted m-silica nanocomposites with different m-silica powder contents with wavenumbers ranging from 4000 to 400 $cm^{-1}$. Figure 8a reveals that the absorption band of the P(NIPAAm-*co*-3 mol % AAc)-grafted m-silica nanocomposites with the 10 wt % m-silica powder at 1640, 1720, 2970, and 3200−3500 $cm^{-1}$ could be assigned to the P(NIPAAm-*co*-3 mol % AAc). The m-silica powder produced peaks at 470, 798, 1103, 1631, 2054, 3070, and 3420 $cm^{-1}$. The absorption band intensity of the P(NIPAAm-*co*-3 mol % AAc) copolymer hydrogels slightly decreased with the increasing m-silica powder content. In particular, a sharp peak became a broad peak at approximately 1130 $cm^{-1}$. These results (Figure 8) agreed more with the XRD (Figure 7), SEM (Figures 5 and 6), and FTIR (Figures 2 and 4) findings than with the earlier analysis results.

TGA was conducted on the P(NIPAAm-*co*-3 mol % AAc)-grafted m-silica nanocomposites to determine the m-silica powder content, as shown in Figure 9. In Figure 9, an initial weight loss was observed up to 120 °C in all composites, which was attributed to the water loss from adsorbed moisture.[52] In the second range, degradation of copolymers containing AAc was observed beginning at 325 °C. AAc units exhibited stepwise thermal decomposition.[53] In the final range, the TGA curves exhibited major decomposition of all nanocomposites in temperatures ranging from 350 to 500 °C, which was attributed to the thermal degradation of the NIPAAm or P(NIPAAm-*co*-3 mol % AAc) copolymer hydrogels.[54] The nearly flat line on the TGA curves indicated no noticeable weight change at 500 to 800 °C. In addition, the P(NIPAAm-*co*-3 mol % AAc)-grafted m-silica nanocomposites had an approximately 10% weight loss at 90 wt % m-silica powder content. The weight loss of the P(NIPAAm-*co*-3 mol % AAc)-grafted m-silica nanocomposites increased from 10 to 90%


https://doi.org/10.1021/acsomega.1c06776
ACS Omega 2022, 7, 8697−8705

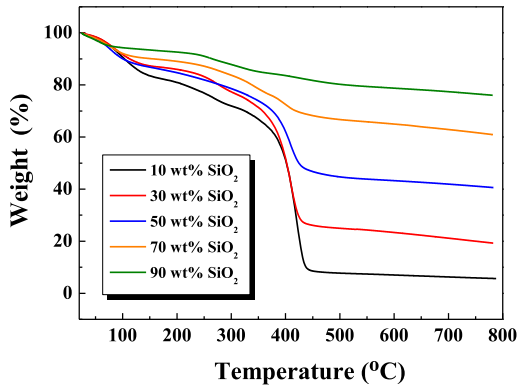


**Figure 9.** TGA analysis of the P(NIPAAm-*co*-3 mol % AAc)-grafted m-silica nanocomposites with different m-silica powders.

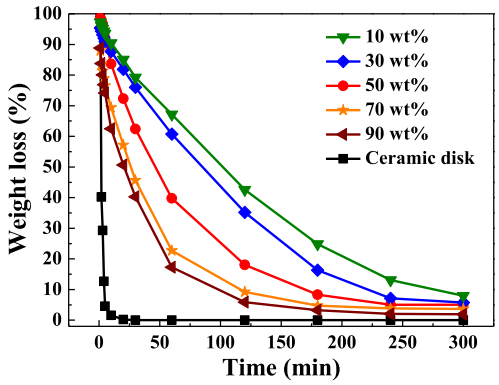


**Figure 10.** Influence of heating time and different m-silica powder content on the deswelling of the P(NIPAAm-*co*-3 mol % AAc)-grafted m-silica nanocomposites.

when the m-silica powder content increased from 10 to 90 wt %. The m-silica powder content corresponded with the design parameter.

**Thermosensitivity of Poly(NIPAAm-*co*-AAc)-Grafted Silica Nanocomposites.** In this study, a thermosensitive P(NIPAAm-*co*-3 mol % AAc)-grafted m-silica nanocomposite was used for smart architectural coatings. Temperature change effects on P(NIPAAm-*co*-3 mol % AAc)-grafted m-silica nanocomposites are a key parameter. Therefore, we simulated outdoor environmental temperature changes during the daytime and nighttime. The uptake of water by the smart architectural coatings occurred at night because the outdoor environmental temperature was lower than the LCST. In addition, the drain water phenomenon from the smart architectural coatings occurred during the daytime as the environmental temperature rose higher than 38 °C (>LCST). Therefore, weight loss from the swelling P(NIPAAm-*co*-3 mol % AAc)-grafted m-silica nanocomposites mixed with different m-silica powder contents were measured at 40 °C (>LCST, noonday temperature in Taiwan) as a function of the heating time in a temperature-programmable testing chamber. The P(NIPAAm-*co*-3 mol % AAc)-grafted m-silica nanocomposites mixed with different m-silica powder contents were screen printed onto the ceramic disk. Next, the P(NIPAAm-*co*-3 mol % AAc)-grafted m-silica nanocomposites mixed with different m-silica powder contents coated on a ceramic disk were immersed in deionized water for 12 h and placed in a temperature-programmable testing chamber.

Figure 10 presents the weight loss of the deswelling P(NIPAAm-*co*-3 mol % AAc)-grafted m-silica nanocomposites as a function of heating time. The P(NIPAAm-*co*-3 mol % AAc)-grafted m-silica nanocomposites were coated on the ceramic disc through screen printing. The weight loss of the noncoated, pure ceramic disc was 100% at a heating time of 10 min. The weight loss of the deswelling P(NIPAAm-*co*-3 mol % AAc)-grafted m-silica nanocomposite mixed with 10 wt % m-silica powder content slightly decreased as the heating time increased. During the 300 min heating time, the weight loss of the deswelling P(NIPAAm-*co*-3 mol % AAc)/10 wt % m-silica nanocomposite was 92.1%. Weight losses of 94.3, 95.2, 96.5, and 98.1% were observed in the deswelling P(NIPAAm-*co*-3 mol % AAc)-grafted m-silica nanocomposite mixed with 30, 50, 70, and 90 wt %, respectively. This result indicated that the P(NIPAAm-*co*-3 mol % AAc)-grafted m-silica nanocomposite could be applied as a smart architectural coating.

To understand the effects of the silica particle size on the deswelling properties of the NIPAAm-*co*-3 mol % AAc-grafted m-silica composite, the micrometer m-silica powder was used in this study. Figure 11 shows the weight loss of the deswelling

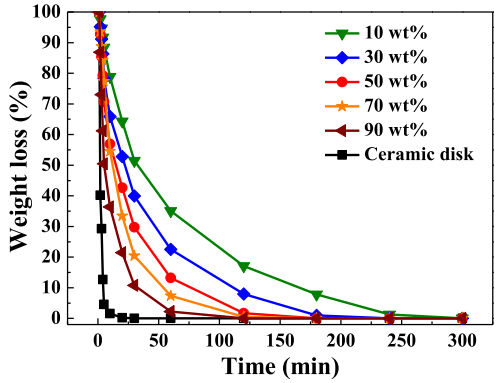


**Figure 11.** Influence of heating time and different microsize m-silica powder content on the deswelling of the P(NIPAAm-*co*-3 mol % AAc)-grafted micrometer m-silica composites.

P(NIPAAm-*co*-3 mol % AAc)-grafted micrometer m-silica composites as a function of heating time. The weight loss of the deswelling P(NIPAAm-*co*-3 mol % AAc)-grafted micrometer m-silica composite mixed with the 10 wt % micrometer m-silica powder decreased as the heating time increased. During the 260 min heating time, the weight loss of the deswelling P(NIPAAm-*co*-3 mol % AAc)-grafted 10 wt % micrometer m-silica composite was 99.5%. The heating time of the deswelling P(NIPAAm-*co*-3 mol % AAc)-grafted 10 wt % m-silica nanocomposite was longer than that of the deswelling P(NIPAAm-*co*-3 mol % AAc)-grafted 10 wt % micrometer m-silica composite. This result is attributable to the specific surface area of the nanosized m-silica powder (Figure 5b) being larger than that of the micrometer m-silica powder (Figure 12a). Therefore, the amount of P(NIPAAm-*co*-3 mol % AAc) copolymers with the same content of coating on the nanometer m-silica powder surface (Figure 6e) is larger than that on the micrometer m-silica powder surface (Figure 12b). In addition, the heating time of the deswelling P(NIPAAm-*co*-3 mol % AAc)-grafted micrometer silica composite rapidly decreased as the micrometer m-silica content increased from 10 to 90 wt %. This result indicated that the P(NIPAAm-*co*-3 mol % AAc)-grafted m-silica nanocomposite could be applied


https://doi.org/10.1021/acsomega.1c06776
ACS Omega 2022, 7, 8697−8705

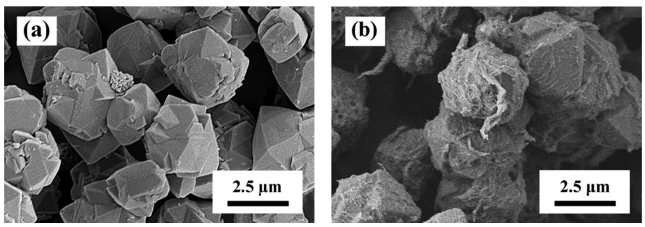


**Figure 12.** SEM images of (a) nonmodified micrometer silica powder and (b) P(NIPAAm-*co*-3 mol % AAc)-grafted 90 wt % micrometer m-silica powder composites.

as a favorable smart architectural coating compared with the P(NIPAAm-*co*-3 mol % AAc)-grafted micrometer m-silica composite.

## CONCLUSIONS

The new class of P(NIPAAm-*co*-3 mol % AAc)-grafted m-silica nanocomposites with a thermosensitive property was investigated. The FTIR results indicated that the silica powder was successfully modified with APTES and ACVA, and enhanced the organic−inorganic interface. In addition, by increasing the AAc concentration from 1 to 9 mol %, the LCST of the P(NIPAAm-*co*-3 mol % AAc) copolymer hydrogels increased from 38 to 68 °C. We selected the 3 mol % AAc hydrogel mixed with NIPAAm hydrogel monomers to form the NIPAAm-*co*-3 mol % AAc hydrogel copolymers, and the LCST of the hydrogel copolymers was 44 °C (12 pm temperature in Taiwan: 36 to 39 °C). As the P(NIPAAm-*co*-3 mol % AAc) copolymers mixed with the 90 wt % m-silica powder, a 98.1% weight loss of the deswelling P(NIPAAm-*co*-3 mol % AAc)-grafted m-silica nanocomposites was observed, even at a heating time of 6 h. In addition, the heating time of the deswelling P(NIPAAm-*co*-3 mol % AAc)-grafted 10 wt % m-silica nanocomposite was longer than that of the deswelling P(NIPAAm-*co*-3 mol % AAc)-grafted 10 wt % micrometer m-silica composite. This result is attributable to the specific surface area of the nanosized m-silica powder being larger than that of the micrometer size m-silica powder. From the abovementioned results, the P(NIPAAm-*co*-3 mol % AAc)-grafted m-silica nanocomposites could be applied on smart architectural coatings. Furthermore, we could control the LCST of the P(NIPAAm-*co*-*x* mol % AAc)-grafted m-silica nanocomposite with different AAc concentrations, which makes it applicable in various environments.

## ASSOCIATED CONTENT

### Supporting Information

The Supporting Information is available free of charge at https://pubs.acs.org/doi/10.1021/acsomega.1c06776.

FTIR spectra of the NIPAAm-*co*-AAc hydrogel copolymers; element mapping images of the NIPAAm-*co*-3 mol % AAc-grafted m-silica nanocomposites; and polymer chains of the NIPAAm (PDF)

## AUTHOR INFORMATION

### Corresponding Author

**Chia-Ching Wu** − *Department of Applied Science, National Taitung University, Taitung 95092 Taiwan, R.O.C.*; orcid.org/0000-0001-8462-5830; Email: ccwu@nttu.edu.tw

### Author

**Chien-Chen Diao** − *Department of Electronic Engineering, Kao Yuan University, Kaohsiung 82151 Taiwan, R.O.C.*

Complete contact information is available at: https://pubs.acs.org/10.1021/acsomega.1c06776

### Author Contributions

C.C.D. and C.C.W. contributed equally to this work.

### Notes

The authors declare no competing financial interest.

## ACKNOWLEDGMENTS

The authors acknowledge the financial support of the Ministry of Science and Technology (MOST 110-2628-E-143-001, MOST 110-2731-M-006-001, and MOST 109-2221-E-143-002-MY2). The authors gratefully acknowledge the use of high-resolution scanning electron microscope (EM003600) and high-temperature 2D X-ray diffractometer (XRD005100) equipment belonging to the Core Facility Center of National Cheng Kung University.

## REFERENCES

(1) Marcotullio, P. J.; Sarzynski, A.; Albrecht, J.; Schulz, N. A Top-down regional assessment of urban greenhouse gas emissions in Europe. *Ambio* **2014**, *43*, 957−968.

(2) Hertwich, E. G.; Wood, R. The growing importance of scope 3 greenhouse gas emissions from industry. *Environ. Res. Lett.* **2018**, *13*, 104013.

(3) De Luca, P.; Carbone, I.; Nagy, J. B. Green Building Materials: a Review of State of the Art Studies of Innovative Materials. *J. Green Build.* **2017**, *12*, 141−161.

(4) Runsheng, T.; Etzion, Y.; Erell, E. Experimental studies on a novel roof pond configuration for the cooling of buildings. *J. Sci. Commun.* **2013**, *28*, 1513−1522.

(5) Han, R.; Xu, Z.; Qing, Y. Study of passive evaporative cooling technique on water-retaining roof brick. *Procedia Eng.* **2017**, *180*, 986−992.

(6) Han, R.; Xu, Z.; Qing, Y.; Long, E. Experimental Research on the Heat Preservation Effect of Water-retaining Roof Bricks in Winter. *Procedia Eng.* **2015**, *121*, 1289−1295.

(7) Kato, T.; Ohashi, K.; Fuji, M.; Takahashi, M. Water absorption and retention of porous ceramics fabricated by waste resources. *J. Ceram. Soc. Jpn.* **2008**, *116*, 212−215.

(8) Ho, C.-H.; Lo, H.-M.; Lin, K.-L.; Lan, J.-Y. Characteristics of water-retaining porous ceramics with sandblasting waste. *Constr. Build. Mater.* **2017**, *157*, 75−82.

(9) Ibrahim, E.; Shao, L.; Riffat, S. B. Performance of porous ceramic evaporators for building cooling application. *Energy Build.* **2003**, *35*, 941−949.

(10) Sugiyama, T.; Kusumoto, K.; Ohashi, M.; Kamiya, A. Environmental Friendly Ceramic Building Materials. *Key Eng. Mater.* **2016**, *690*, 150−155.

(11) Thu, H. T. M.; Sato, H. Proposal of an Eco-Friendly High-Performance Air-Conditioning System. Part 1. Possibility of Improving Existing Air-Conditioning System by an Evapo-Transpiration Condenser. *Int. J. Refrig.* **2013**, *36*, 1589−1595.

(12) Thu, H. T. M.; Sato, H. Proposal of an eco-friendly high-performance air-conditioning system part 2. Application of evapo-transpiration condenser to residential air-conditioning system. *Int. J. Refrig.* **2013**, *36*, 1596−1601.

(13) Aimiuwu, V. O. Evaporative Cooling of Water in Hot Arid Regions. *Energy Convers. Manage.* **1992**, *33*, 69−74.

(14) Mohan, B.; Konatham, S. Advanced Hollow Pipes Made of Ceramic Air Cooler. *IJMETMR* **2016**, *3*, 72−77.

(15) He, J.; Hoyano, A. Experimental Study of Cooling Effects of a Passive Evaporative Cooling Wall Constructed of Porous Ceramics

with High Water Soaking-up Ability. *Build. Environ.* **2010**, *45*, 461−472.
(16) Chen, W.; Liu, S.; Lin, J. Analysis on the Passive Evaporative Cooling Wall Constructed of Porous Ceramic Pipes with Water Sucking Ability. *Energy Build.* **2015**, *86*, 541−549.
(17) Okada, K.; Ooyama, A.; Isobe, T.; Kameshima, Y.; Nakajima, A.; MacKenzie, K. J. D. Water retention properties of porous geopolymers for use in cooling applications. *J. Eur. Ceram. Soc.* **2009**, *29*, 1917−1923.
(18) Zou, D.; Li, K.; Li, W.; Li, H.; Cao, T. Effects of pore structure and water absorption on internal curing efficiency of porous aggregates. *Constr. Build. Mater.* **2018**, *163*, 949−959.
(19) Okada, K.; Matsui, S.; Isobe, T.; Kameshima, Y.; Nakajima, A. Water-retention properties of porous ceramics prepared from mixtures of allophane and vermiculite for materials to counteract heat island effects. *Ceram. Int.* **2008**, *34*, 345−350.
(20) Lin, K.-L.; Lan, J.-Y. Porous Ceramic Characteristics Sintered from Waste Diatomite and Sodium Silicate Sand. *Int. J. Mater., Mech. Manuf.* **2013**, *1*, 240−244.
(21) Janetti, M. B.; Janssen, H. Impact of the drying rate on the moisture retention curve of porous building materials. *Constr. Build. Mater.* **2020**, *258*, 119451.
(22) Katsuki, H.; Choi, E. K.; Lee, W. J.; Kim, U. S.; Hwang, K. T.; Cho, W. S. Eco-friendly Self-cooling System of Porous Onggi Ceramic Plate by Evaporation of Absorbed Water. *J. Korean Ceram. Soc.* **2018**, *55*, 153∼159.
(23) Dutra, L. F.; Freitas, M. E.; Grillet, A. C.; Mendes, N.; Woloszyn, M. Microstructural Characterization of Porous Clay-Based Ceramic Composites. *Materials* **2019**, *12*, 946.
(24) Heskins, M.; Guillet, J. E. Solution properties of poly(N-isopropylacrylamide). *J. Macromol. Sci., Part A: Pure Appl.Chem.* **1968**, *2*, 1441−1455.
(25) Hirokawa, Y.; Tanaka, T. J. Volume phase transition in a nonionic gel. *Chem. Phys.* **1984**, *81*, 6379−6380.
(26) Zhang, X.-Z.; Yang, Y.-Y.; Chung, T.-S.; Ma, K.-X. Preparation and Characterization of Fast Response Macroporous Poly(N-isopropylacrylamide) Hydrogels. *Langm* **2001**, *17*, 6094.
(27) Kayaman, N.; Kazan, D.; Erarslan, A.; Okay, O.; Baysal, B. M. Structure and protein separation efficiency of poly(N-isopropylacrylamide) gels: Effect of synthesis conditions. *J. Appl. Polym. Sci.* **1998**, *67*, 805−814.
(28) Kim, Y. K.; Kim, E.-J.; Lim, J. H.; Cho, H. K.; Hong, W. J.; Jeon, H. H.; Chung, B. G. Dual Stimuli-Triggered Nanogels in Response to Temperature and pH Changes for Controlled Drug Release. *Nanoscale Res. Lett.* **2019**, *14*, 77.
(29) Yu, J.; Yang, L.; Liang, X.; Dong, T.; Qu, H.; Rong, M.; Liu, H. Aptamer and PNIPAAm co-conjugated nanoparticles regulate activity of enzyme with different temperature. *Talanta* **2016**, *159*, 47−54.
(30) Cetintas, M.; de Grooth, J.; Hofman, A. H.; van der Kooij, H. M.; Loos, K.; de Vos, W. M.; Kamperman, M. Free-standing thermo-responsive nanoporous membranes from high molecular weight PS-PNIPAM block copolymers synthesized via RAFT polymerization. *Polym. Chem.* **2017**, *8*, 2235−2243.
(31) Lin, X.; Tang, D.; Yu, Z.; Feng, Q. Stimuli-responsive electrospun nanofibers from poly(N-isopropylacrylamide)-co-poly-(acrylic acid) copolymer and polyurethane. *J. Mater. Chem. B* **2014**, *2*, 651−658.
(32) Lue, S. J.; Chen, C.-H.; Shih, C.-M. Tuning of Lower Critical Solution Temperature (LCST) of Poly(N-Isopropylacrylamide-co-Acrylic acid) Hydrogels. *J. Macromol. Sci., Part B: Phys.* **2011**, *50*, 563−579.
(33) Kim, Y. K.; Kim, E. J.; Lim, J. H.; Cho, H. K.; Hong, W. J.; Jeon, H. H.; Chung, B. G. Dual stimuli-triggered nanogels in response to temperature and pH changes for controlled drug release. *Nanoscale Res. Lett.* **2019**, *14*, 77.
(34) Rzaev, Z. M. O.; Dinçer, S.; Pişkin, E. Functional copolymers of N-isopropylacrylamide for bioengineering applications. *Prog. Polym. Sci.* **2007**, *32*, 534−595.
(35) Liu, H.; Liu, M.; Jin, S.; Chen, S. Synthesis and characterization of fast responsive thermo- and pH-sensitive poly[(N,N-diethylacrylamide)-co-(acrylic acid)] hydrogels. *Polym. Int.* **2008**, *57*, 1165−1173.
(36) Gemeinhart, R. A.; Park, H.; Park, K. Pore structure of superporous hydrogels. *Polym. Adv. Technol.* **2000**, *11*, 617−625.
(37) Ghosh Chaudhuri, R.; Paria, S. Core/shell nanoparticles: classes, properties, synthesis mechanisms, characterization, and applications. *Chem. Rev.* **2011**, *112*, 2373−2433.
(38) Rahman, I. A.; Padavettan, V. Synthesis of Silica Nanoparticles by Sol-Gel: Size-Dependent Properties, Surface Modification, and Applications in Silica-Polymer Nanocomposites-A Review. *J. Nanomater.* **2012**, *2012*, 1−15.
(39) Mallakpour, S.; Naghdi, M. Fabrication and characterization of novel polyvinylpyrrolidone nanocomposites having $SiO_2$ nanoparticles modified with citric acid and L (+)-ascorbic acid. *Polymer* **2016**, *90*, 295−301.
(40) Sarikhani, K.; Jeddi, K.; Thompson, R. B.; Park, C. B.; Chen, P. Adsorption of Surface-Modified Silica Nanoparticles to the Interface of Melt Poly(lactic acid) and Supercritical Carbon Dioxide. *Langmuir* **2015**, *31*, 5571−5579.
(41) Gurunathan, T.; Chung, J. S. Synthesis of aminosilane crosslinked cationomeric waterborne polyurethane nanocomposites and its physicochemical properties. *Colloids Surf., A* **2017**, *522*, 124−132.
(42) Saengdee, P.; Chaisriratanakul, W.; Bunjongpru, W.; Sripumkhai, W.; Srisuwan, A.; Jeamsaksiri, W.; Hruanun, C.; Poyai, A.; Promptmas, C. Surface modification of silicon dioxide, silicon nitride and titanium oxynitride for lactate dehydrogenase immobilization. *Biosens. Bioelectron.* **2015**, *67*, 134−138.
(43) Lai, S.; Chen, G.; Hu, W.; Liu, B.; Yang, X.; Gao, K. Preparation and performance of DOPO-nano-$SiO_2$ modified poly-acrylic acid-based flame retardant dust suppressant for coal. *New J. Chem.* **2021**, *45*, 17461−17474.
(44) Lin, C.; Lü, T.; Qi, D.; Cao, Z.; Sun, Y.; Wang, Y. Effects of Surface Groups on $SiO_2$ Nanoparticles on in Situ Solution Polymerization: Kinetics and Mechanism. *Ind. Eng. Chem. Res.* **2018**, *57*, 15280−15290.
(45) Ma, G.; Luo, X.; Sun, X.; Wang, W.; Shou, Q.; Liang, X.; Liu, H. Glycopolymer Grafted Silica Gel as Chromatographic Packing Materials. *Int. J. Mol. Sci.* **2019**, *20*, 10.
(46) da Silva, R.; Ganzarolli de Oliveira, M. Effect of the cross-linking degree on the morphology of poly(NIPAAm-co-AAc) hydrogels. *Polymer* **2007**, *48*, 4114−4122.
(47) Guo, W.; Lu, C.-H.; Qi, X.-J.; Orbach, R.; Fadeev, M.; Yang, H.-H.; Willner, I. Switchable bifunctional stimuli-triggered poly-N-isopropylacrylamide/DNA hydrogels. *Angew. Chem., Int. Ed.* **2014**, *53*, 10134−10138.
(48) Wang, J.; Pan, X.; Wang, S. Preparation and characterization of polyglutamic/chitosan/nano-silver composite hydrogels. *Ion Exch. Adsorpt.* **2016**, *32*, 297−305.
(49) Zhang, M.; Li, Y.; Yang, Q.; Huang, L.; Chen, L.; Ni, Y.; Xiao, H. Temperature and pH responsive cellulose filament/poly (NIPAM-co-AAc) hybrids as novel adsorbent towards Pb(II) removal. *Carbohydr. Polym.* **2018**, *195*, 495−504.
(50) Cueto-Díaz, E. J.; Castro-Muñiz, A.; Suárez-García, F.; Gálvez-Martínez, S.; Torquemada-Vico, M. C.; Valles-González, M. P.; Mateo-Martí, E. APTES-Based Silica Nanoparticles as a Potential Modifier for the Selective Sequestration of $CO_2$ Gas Molecules. *Nanomaterials* **2021**, *11*, 2893.
(51) Suzuki, K.; Yumura, T.; Mizuguchi, M.; Tanaka, Y.; Chen, C.-W.; Akashi, M. Poly(N-isopropylacrylamide)-Grafted Silica as a Support of Platinum Colloids: Preparation Method, Characterization, and Catalytic Properties in Hydrogenation. *J. Appl. Polym. Sci.* **2000**, *77*, 2678−2684.
(52) Zhang, J.; Wang, Q.; Wang, A. Synthesis and characterization of chitosan-g-poly(acrylic acid)/attapulgite superabsorbent composites. *Carbohydr. Polym.* **2007**, *68*, 367−374.


https://doi.org/10.1021/acsomega.1c06776
*ACS Omega* 2022, 7, 8697−8705

(53) Dubinsky, S.; Lumelsky, Y.; Grader, G. S.; Shter, G. E.; Silverstein, M. S. Thermal degradation of poly(acrylic acid) containing metal nitrates and the formation of $YBa_2Cu_3O_{7-x}$. *J. Polym. Sci., Part B: Polym. Phys.* **2005**, *43*, 1168−1176.
(54) Picos-Corrales, L. A.; Licea-Claverie, A.; Cornejo-Bravo, J. M.; Schwarz, S.; Arndt, K.-F. Well-defined N -Isopropylacrylamide Dual-Sensitive Copolymers with LCST ≈38 °C in Different Architectures: Linear, Block and Star Polymers. *Macromol. Chem. Phys.* **2012**, *213*, 301−314.



https://doi.org/10.1021/acsomega.1c06776
*ACS Omega* 2022, 7, 8697−8705